

The emergence of perovskite solar cells

Martin A. Green^{1*}, Anita Ho-Baillie¹ and Henry J. Snaith²

The past two years have seen the unprecedentedly rapid emergence of a new class of solar cell based on mixed organic–inorganic halide perovskites. Although the first efficient solid-state perovskite cells were reported only in mid-2012, extremely rapid progress was made during 2013 with energy conversion efficiencies reaching a confirmed 16.2% at the end of the year. This increased to a confirmed efficiency of 17.9% in early 2014, with unconfirmed values as high as 19.3% claimed. Moreover, a broad range of different fabrication approaches and device concepts is represented among the highest performing devices — this diversity suggests that performance is still far from fully optimized. This Review briefly outlines notable achievements to date, describes the unique attributes of these perovskites leading to their rapid emergence and discusses challenges facing the successful development and commercialization of perovskite solar cells.

Recent substantial reductions in the manufacturing costs of mainstream silicon solar cell technology assure the future large-scale use of photovoltaics, with a recent forecast anticipating photovoltaics will contribute nearly a third of new electricity generation capacity worldwide between now and 2030¹. As in microelectronics, silicon has a combination of strengths that has made it difficult to displace as the favoured photovoltaic material. Opportunities exist for technologies that promise either significantly higher energy conversion efficiencies or significantly lower processing costs. A new generation of mixed organic–inorganic halide perovskites offers tantalizing prospects on both fronts^{2–6}.

Some key attributes of these perovskites include ease of fabrication, strong solar absorption and low non-radiative carrier recombination rates for such simply prepared materials, plus the ability to capitalize on over 20 years of development of related dye-sensitized and organic photovoltaic cells. A reasonably high carrier mobility is an important property for some cell architectures, as is the range of properties accessible by forming mixed compounds within a compatible materials system. One negative aspect of perovskites is the fact that lead has been a major constituent of all highly performing perovskite cells to date, raising toxicity issues during device fabrication, deployment and disposal. Also, they generally undergo degradation (sometimes quite rapid) on exposure to moisture and ultraviolet radiation.

Perovskites are materials described by the formula ABX_3 , where X is an anion and A and B are cations of different sizes (A being larger than B). The crystal structure of perovskites is depicted in Fig. 1a. Their crystallographic stability and probable structure can be deduced by considering a tolerance factor t and an octahedral factor μ (ref. 7); here, t is defined as the ratio of the distance A–X to the distance B–X in an idealized solid-sphere model ($t = (R_A + R_X) / \{\sqrt{2}(R_B + R_X)\}$, where R_A , R_B and R_X are the ionic radii of the corresponding ions) and μ is defined as the ratio R_B/R_X . For halide perovskites ($X = F, Cl, Br, I$), generally $0.81 < t < 1.11$ and $0.44 < \mu < 0.90$. If t lies in the narrower range 0.89–1.0, the cubic structure of Fig. 1a is likely, with lower t values giving less symmetric tetragonal or orthorhombic structures. Despite these constraints, transitions between such structures on heating are common for any given perovskite, with the high-temperature phase generally being cubic.

For the organic–inorganic halide perovskites of present interest, the larger cation A is organic; it is generally methylammonium ($CH_3NH_3^+$) with $R_A = 0.18$ nm (ref. 8), although related

ethylammonium ($CH_3CH_2NH_3^+$) ($R_A = 0.23$ nm)⁹ and formamidinium ($NH_2CH=NH_2^+$) (R_A is estimated to lie in the range 0.19–0.22 nm) also give good results^{10–13}. The anion X is a halogen, generally iodine ($R_X = 0.220$ nm), although Br and Cl are also commonly used ($R_X = 0.196$ nm and 0.181 nm), usually in a mixed halide material. For efficient cells, cation B has universally been Pb ($R_B = 0.119$ nm); Sn ($R_B = 0.110$ nm) forms similar compounds with lower, theoretically more ideal bandgaps¹⁴, but generally lower stability (attributed to the ease of oxidation of Sn to SnI_4 in the iodide perovskite; relativistic effects in the Pb counterpart are thought to provide greater protection against oxidation¹⁴). The archetypal compound is thus methylammonium lead triiodide ($CH_3NH_3PbI_3$), with mixed halides $CH_3NH_3PbI_{3-x}Cl_x$ and $CH_3NH_3PbI_{3-x}Br_x$ also being important. Calculated and estimated t and μ factors for a range of these perovskites are shown in Fig. 1b.

Notable achievements to date

Interest in organic–inorganic halide perovskites dates back over a century¹⁵, although present results benefit from recent investigations of related thin-film transistors and light-emitting diodes (LEDs) by Mitzi and co-workers^{16,17}. Although these LEDs doubtless exhibited photovoltaic properties and their use in solar cells was anticipated¹⁷, this was not studied at the time, partly because of Pb toxicity and the fact that more benign Sn materials were not considered to be sufficiently robust (D. Mitzi, personal communication).

Miyasaka and co-workers^{18–20} were apparently the first to report photovoltaic results for perovskites; they were attracted by the self-organization potential of perovskite in the nanoporous TiO_2 layer of dye-sensitized cells. In 2006, they reported $CH_3NH_3PbBr_3$ cells with an efficiency of 2.2% (ref. 18); by replacing bromine with iodine they were able to increase the efficiency to 3.8% in 2009¹⁹ (although all devices were unstable). An organic electrolyte containing lithium halide and the corresponding halogen formed the hole-transporting medium (HTM), allowing positive contact. Attempts to replace this HTM with a solid-state HTM were not particularly successful²⁰.

Subsequently, Park and colleagues²¹ employed similar structures in which perovskite was shown to be deposited as sparsely spaced hemispherical nanoparticles that were approximately 2.5 nm in diameter. By applying TiO_2 surface treatment prior to deposition, they realized an efficiency of 6.5% in 2011²¹. Perovskite nanoparticles exhibited better absorption than standard N719 dye sensitizers,

¹Australian Centre for Advanced Photovoltaics (ACAP), School of Photovoltaic and Renewable Energy Engineering, University of New South Wales, Sydney 2052, Australia. ²University of Oxford, Clarendon Laboratory, Parks Road, Oxford OX1 3PU, UK. *e-mail: m.green@unsw.edu.au

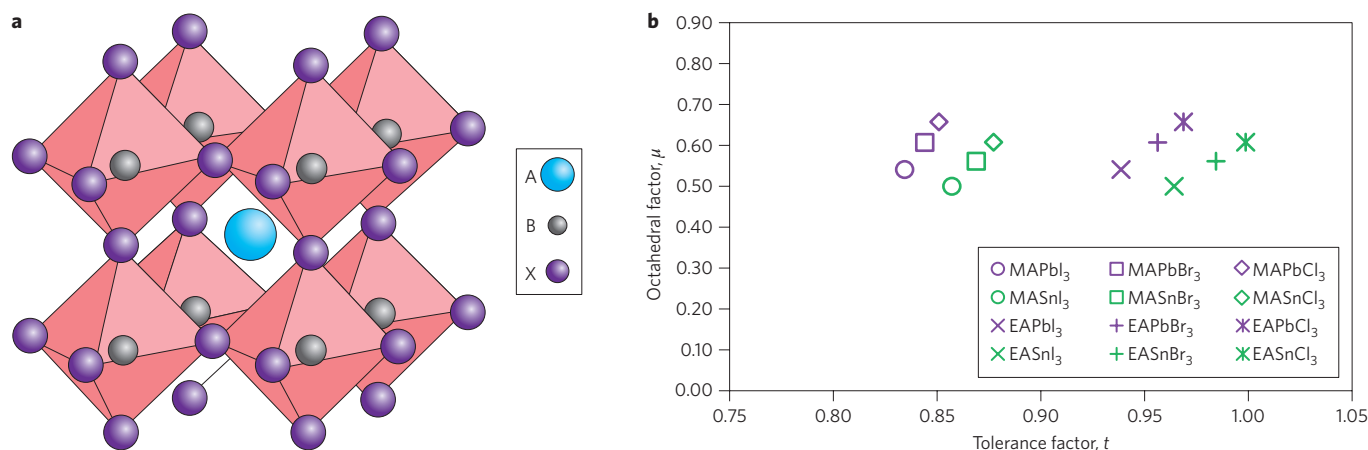


Figure 1 | Perovskite crystal structure and associated tolerance and octahedral factors. **a**, Cubic perovskite crystal structure. For photovoltaically interesting perovskites, the large cation A is usually the methylammonium ion (CH_3NH_3), the small cation B is Pb and the anion X is a halogen ion (usually I, but both Cl and Br are also of interest). For $\text{CH}_3\text{NH}_3\text{PbI}_3$, the cubic phase forms only at temperatures above 330 K due to a low t factor (0.83). **b**, Calculated t and μ factors for 12 halide perovskites. The corresponding formamidinium ($\text{NH}_2\text{CH}=\text{NH}_2$) based halides are expected to have intermediate values between those of the methylammonium (MA) and ethylammonium (EA; $\text{CH}_3\text{CH}_2\text{NH}_3$) compounds shown.

but they dissolved in the electrolyte, resulting in a rapid degradation of performance²¹.

This stimulated the replacement of problematic electrolytes by a solid-state HTM^{22,23}. Park, Grätzel and colleagues²² introduced a spiro-MeOTAD (2,2',7,7'-tetrakis(N,N-di-p-methoxyphenylamine)-9,9'-spirobifluorene) HTM, which was developed for organic LEDs²⁴ but was also found to be effective in solid-state dye cells²⁵. When dissolved in an organic solvent, spiro-MeOTAD penetrates nanoporous TiO_2 , leaving only solute molecules after solvent evaporation. Spiro-MeOTAD not only improved the stability, as expected, it also boosted the reported efficiency to 9.7% (ref. 22). The cell structure is encompassed by the more general device of Fig. 2a if the optional continuous perovskite layer is removed, leaving only scaffolding infiltrated by perovskite (and subsequently HTM).

Almost simultaneously (mid-2012), Snaith and co-workers²³ also reported success with spiro-MeOTAD along with four additional developments that split the field wide open. One of these developments was the use of the mixed-halide $\text{CH}_3\text{NH}_3\text{PbI}_{3-x}\text{Cl}_x$, which exhibited better stability and carrier transport than its pure iodide equivalent^{23,26}. A second involved going beyond earlier nanoparticle structures by coating nanoporous TiO_2 surfaces with a thin perovskite layer and thereby forming extremely thin absorber (ETA) cells. A third was replacing conducting nanoporous TiO_2 by a similar but non-conducting Al_2O_3 network. This improved the open-circuit voltage (V_{oc}), boosting the reported efficiency to 10.9%; it also demonstrated that perovskites have a broader potential than just being used as sensitizers, as they are able to transport both electrons and holes between cell terminals. The fourth development exploited such ambipolar transport by demonstrating simple planar cells with the scaffolding (Fig. 2a) completely eliminated.

A jump to a reported efficiency of 12.0% came from the combined efforts of Seok, Grätzel and colleagues using both optional layers shown in Fig. 2a, including a solid perovskite capping layer overlying the scaffolding²⁷ (nanoporous TiO_2 infiltrated by perovskite). Of the HTMs they investigated (which included spiro-MeOTAD), poly-triarylamine proved to be the best. Seok's group further improved the performance to realize a reported efficiency of 12.3% using similar structures and mixed-halide $\text{CH}_3\text{NH}_3\text{PbI}_{3-x}\text{Br}_x$ perovskites²⁸. A low Br content (<10%) gave the best initial efficiency due to a lower bandgap, but higher Br contents (>20%) provided a better high-humidity stability. This was correlated with a tetragonal to pseudo-cubic structural transition arising from a

higher t factor due to the smaller ionic radius of Br (molecules in position A exclude full cubic symmetry²⁹).

Further progress was reported at the European Materials Research Symposium in May 2013, with two groups reporting efficiencies above 15%. Grätzel's group used TiO_2 scaffolding and two-step iodide deposition, which improved the morphology³⁰. They also reported the first independent measurements of efficiency by an independent accredited test centre, which confirmed an efficiency of 14.1%. (Independent measurements were found to be an essential quality-control measure with other photovoltaic technologies to prevent inflated results infiltrating the literature³¹; inexperience or overenthusiasm often result in 'in-house' data being overestimates.) Snaith's group reported similar results using vastly different planar cells that did not have scaffolding. The simpler structure allowed $\text{CH}_3\text{NH}_3\text{PbI}_{3-x}\text{Cl}_x$ deposition by two-source thermal evaporation, again giving a better morphology³² and a reported efficiency of 15.4%.

No efficiency improvements were announced at the 2013 Fall Materials Research Society (MRS) Meeting, although a special perovskite session attracted considerable attention. At the end of 2013, Seok's group achieved an independently confirmed efficiency of 16.2% by using the mixed-halide $\text{CH}_3\text{NH}_3\text{PbI}_{3-x}\text{Br}_x$ (10–15% Br) and a poly-triarylamine HTM (S. I. Seok, personal communication). Both optional layers shown in Fig. 2a were included, with the thickness ratio of perovskite-infiltrated TiO_2 scaffolding relative to the continuous perovskite layer being the key to the improved efficiency (S. I. Seok, personal communication). This was increased to a confirmed efficiency of 17.9% in early 2014 (S. I. Seok, personal communication). An unconfirmed efficiency of 19.3% was reported at the 2014 Spring MRS Meeting⁶ (some uncertainty surrounds this reported efficiency due to the absence of supporting information).

Significantly, the latter three results were obtained using device structures that span all the possibilities inherent in Fig. 2a: one or both optional layers, three different mixed-halide perovskites and two different HTMs were used (although some ambiguities remain^{30,33}). Fabrication simplicity combined with similarities with dye-sensitized and organic photovoltaics has resulted in a rapid increase in the number of researchers working in this field. Before 2013, only seven journal papers had been published that discussed photovoltaic devices based on halide perovskites, whereas by the end of 2013, relevant publications were appearing at the rate of seven per month. This spurt further increased the diversity of approaches that gave creditable performances.

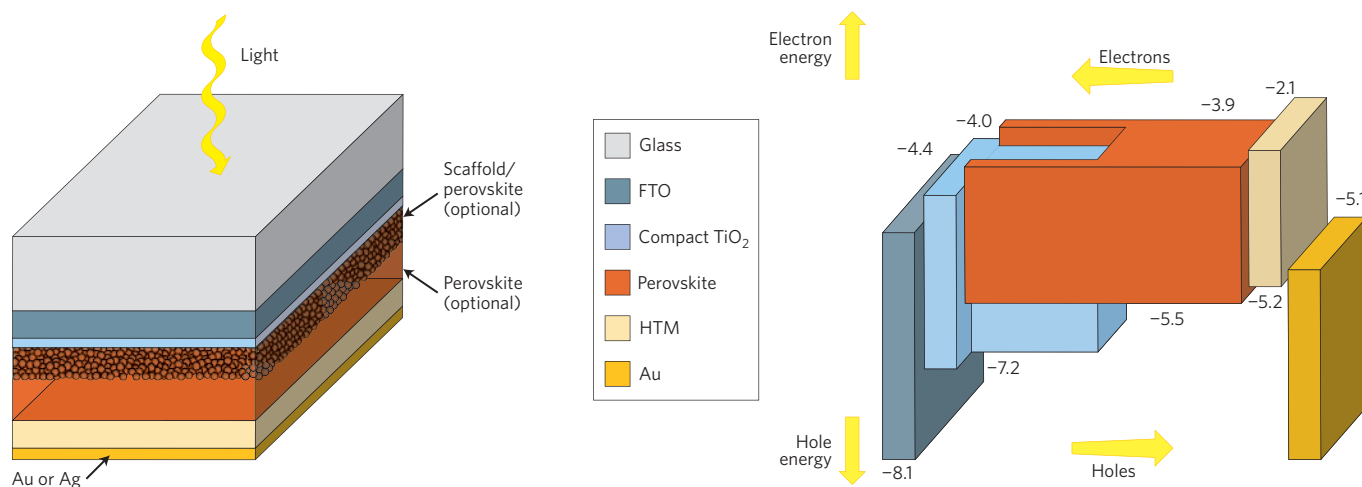


Figure 2 | Perovskite cell structure and associated vacuum energy levels. **a**, General organic-inorganic halide solar cell, which includes two optional layers that are not essential for high performance; an energy conversion efficiency of over 15% has been reported for devices that have both optional layers, with only the scaffold layer infiltrated by the perovskite (and then by the HTM) and without scaffolding; the structure then corresponds to a simple planar thin-film cell. **b**, Vacuum energy levels (in eV) for corresponding materials (CH₃NH₃PbI₃ perovskite, conducting TiO₂ scaffold).

Key recent results include demonstrations of an additional deposition process involving PbI₂ deposition from solution with *in situ* conversion to perovskite by a vapour-phase CH₃NH₃I reaction³⁴. Promising results have also been reported with perovskites based on organic cations other than CH₃NH₃⁺. Cations with larger ionic radii, specifically ethylammonium (CH₃CH₂NH₃⁺)¹⁰ and formamidinium (NH₂CH=NH₂⁺)^{11–13}, increase the *t* factor and push structures towards the symmetrical cubic phase. Different proportions of organic cations, inorganic cations (Pb, Sn) and halide anions (I, Br, Cl) can be incorporated in mixed perovskites, allowing their properties to be fine-tuned; however, the use of mixed halides has dominated.

Recent work has also demonstrated the use of new HTMs and electron transport media (ETMs). Effective ETMs have been reported in which the standard fluorine-doped tin oxide (FTO)/compact TiO₂ combination is replaced by indium tin oxide as a transparent conducting oxide combined with a thin (25 nm) ZnO-nanoparticle layer³⁵; this gave a reported efficiency of 15.7% for planar cells on glass. Low-temperature processing also gave a creditable performance on flexible polyethylene terephthalate. Inorganic HTMs such as CuI³⁶ and CuSCN³⁷ also give reasonable results, as do organic-photovoltaic-derived organics for both ETMs and HTMs, specifically a (6,6)-phenyl C₆₁-butyric acid methyl ester ETM combined with a poly(2,3-dihydrothieno-1,4-dioxin)-poly(styrenesulphonate) HTM^{38–40} (efficiencies up to 12%, refs 38,39).

Such diversification increases potential applications. Flexible cells⁵ require low processing temperatures of less than 150 °C, rather than 500 °C, which is typical for compact TiO₂. Graphene nanoflakes in the normally compact TiO₂ layer allow such processing⁴¹. An efficiency of 15.6% has been reported for a structure that includes all optional layers and Al₂O₃ scaffolding (0.6% graphene/TiO₂ by weight)⁴¹, and an efficiency of 15.9% has been achieved by combining small TiO₂ nanoparticles with a titanium diisopropoxide bis(acetylacetonate) binder⁴². In other work, the non-uniformity produced by solution deposition is exploited to produce neutral-colour semi-transparent cells⁴³. Instead of continuous perovskite, small invisible islands are grown, which should be less expensive than laser approaches for fabricating semi-transparent amorphous-silicon cells⁴⁴.

Enabling attributes

Strong optical absorption is the key to the outstanding performance of these perovskite cells, reducing both the required thickness and

the challenges in collecting photogenerated carriers. Absorption measurements (Fig. 3a) are consistent with calculations showing direct-bandgap properties for perovskites of interest^{14,45}. Two strong, spin-orbit split, excitonic absorption thresholds are apparent, as in direct-bandgap III–V semiconductors⁴⁶. However, reverse ordering of band-edge states (specifically a p-like conduction band)⁴⁷ results in splitting in the conduction band, rather than in the valence band. Interestingly, reverse band-edge ordering also gives a bandgap that increases with increasing temperature for any given phase^{48,49}, which is the opposite trend to that of tetrahedrally coordinated semiconductors.

The strong excitonic absorption edge also means there is no basis for the common practice of determining bandgaps using Tauc plots⁵⁰. The absorption edge is determined by a broadened exciton impulse response, as is the case for direct III–V semiconductors, with the unbroadened response described by Elliott's theory^{46,51}. The relatively high exciton binding energy compared to those of III–V semiconductors with a similar bandgap (37–50 meV has been reported for iodide in the low-temperature phase⁵² and 35–75 meV for the mixed chloride at room temperature⁴⁹), not only lowers the absorption threshold, but also increases the strength of the above-bandgap absorption that generates unbound electron–hole pairs. Correspondingly, above-bandgap absorption is comparable to or stronger than that in many direct-bandgap III–V semiconductors, such as GaAs, although it is lower than that of some inorganic chalcogenides (see Fig. 3a).

For devices with a continuous perovskite layer or an insulating scaffold (Fig. 2a), transport across the perovskite is important for device operation. The exciton binding energy is still sufficiently low for photogeneration of both excitons and unbound electron–hole pairs, with thermal dissociation of excitons into free carriers (and reassociation into excitons) expected. The respective photocurrent contributions ideally depend on the coupling between these populations, as characterized by the intrinsic exciton dissociation time — the time that would prevail if excitons were not mobile or could not be ionized at heterojunctions.

At the low-coupling extreme (dissociation times large compared to recombination times), the two populations will be independent and relative concentrations will be determined by the spectral composition of illumination. For sunlight, free electron–hole pair generation is expected to be completely dominant, as primary exciton generation will occur only at wavelengths near band edges (at least

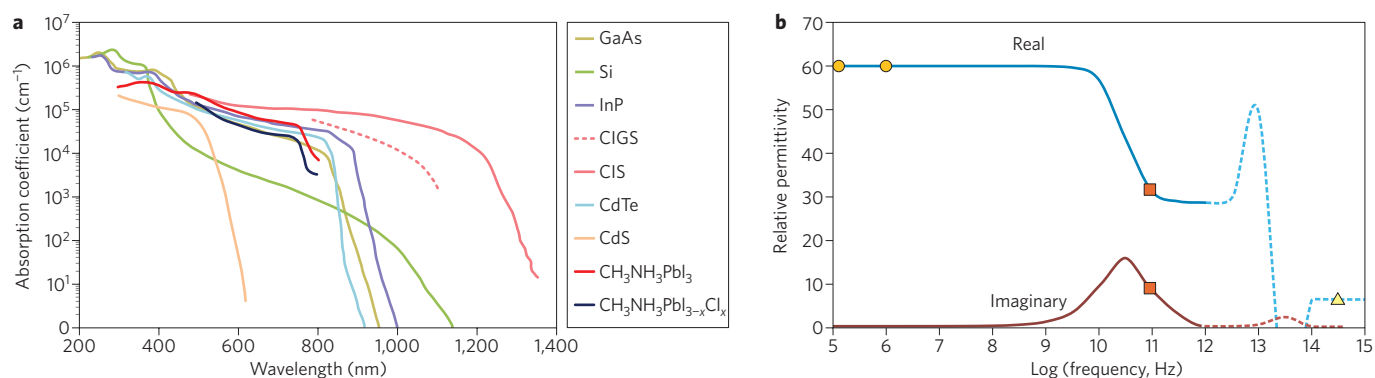


Figure 3 | Absorption coefficients and relative permittivity. **a**, Absorption coefficient of CH₃NH₃PbI₃ (ref. 40) (these values are about 50% higher than those obtained by Xing *et al.*⁷⁴) and CH₃NH₃PbI_{3-x}Cl_x (ref. 96) compared to other solar cell materials (various sources). **b**, Real and imaginary parts of the CH₃NH₃PbI₃ dielectric constant at 300 K as a function of frequency. Dipolar and ionic components successively disappear as the frequency increases. Low-frequency values (circles) are from ref. 64, mid-frequency (90 GHz) values (squares) are from ref. 65 and optical-frequency value (triangle) is from ref. 66. The solid lines are Debye relaxation fits to mid-range values (ref. 65). The dashed lines show possible transitional values in the far infrared (qualitative only).

for continuous perovskite layers). To contribute to the photocurrent in this low-coupling limit, excitons would need to dissociate at an interface (that with the ETM or the HTM or both), as in organic photovoltaic devices.

At the opposite extreme of high coupling (rapid dissociation), free electron-hole and exciton concentrations will equilibrate with relative concentrations theoretically determined by a mass action law rather than by the illumination (this law will take the form deduced by Combescot^{53,54}, when corrected to account for excited exciton states and scattering states associated with electron-hole attraction⁵⁵). Excitons are expected to flow in the same direction as electrons or holes (Fig. 2b), depending on which has the larger electrochemical gradient⁵⁶. Because electron and hole currents increase in opposite directions (Fig. 2b), these gradients will probably be equal at one point in the device, where the total flux is free carriers. No additional exciton dissociation features will be required in this case. Transport could then be treated as free carrier with transport and recombination parameters determined by a weighted combination of free carrier and excitonic values⁵⁶. For a relatively narrow coupling range lying between the low and high extremes, intermediate behaviour is expected⁵⁴. As well as strengthening absorption, excitons provide an additional pool of carriers that may assist carrier transport. Benefits are expected if the lifetime of exciton diffusion or recombination exceeds that of free carriers⁵⁴. However, despite relatively high exciton binding energies and uncertainties arising from attempting to separate correlated electron-hole pairs into bound and scattering states⁵⁵, it seems as if exciton concentrations will be low compared to both free-carrier concentrations except in extreme circumstances, a conclusion supported by a recently published work⁴⁹.

Another striking attribute of these perovskites is their low non-radiative recombination rates compared to other thin-film polycrystalline semiconductors. This property manifests itself in the relatively small difference between V_{oc} of experimental cells and their effective bandgap potential³ (E_g/q) or alternatively by their high external radiative efficiency, a parameter deducible from V_{oc} and the spectral response⁵⁷. The best perovskite cells have relatively low values for the difference $E_g/q - V_{oc}$ (about 450 meV, ref. 3) and relatively high calculated external radiative efficiencies (0.058%; I. Al Mansouri, personal communication). This makes perovskites particularly interesting for high E_g cells in tandem cell stacks³, where the high V_{oc} values of such cells give rise to substantial efficiency advantages. The diverse range of fabrication methods that have been used, which include low-temperature approaches, further enhances the prospects of these perovskites as a tandem cell component.

In conventional polycrystalline semiconductors, low non-radiative recombination generally requires large grain sizes, a low grain-boundary activity and a low density of intragranular defects. The present perovskites give narrow X-ray diffraction peaks that are consistent with both near micrometre grain sizes and a reasonably low intergranular defect density⁵⁸. Large grain sizes might be expected from the high 'effective' homologous temperatures corresponding to relatively low processing temperatures due to the low imputed perovskite melting points (most decompose before melting²⁹). For metals, a 0.2 increase in the homologous temperature increases the grain size by a factor of ten⁵⁹. To reduce detrimental grain boundary activity, specific processing steps are required for polycrystalline Si, CdTe and copper-indium-gallium diselenide (CIGS) cells. These perovskites do not seem to require such processing steps⁶⁰. This may be because of their high effective homologous temperatures, the tendency for the inorganic planes to align parallel to substrates⁶¹ (which reduces one degree of misorientations), crystallographic flexibility (allowing more graceful accommodation of misorientations than in more rigid materials), or a combination of all these factors.

A recent study⁶² investigated the activity of intrinsic intergranular defects in CH₃NH₃PbI₃ using density functional theory. Two types of intrinsic defects were studied: neutral Schottky defects (equal number of positive and negative vacancies) and Frenkel defects (equal number of vacancies and interstitials of the same ion). Schottky defects, such as PbI₂ and CH₃NH₃I vacancies, were found not to generate defect states having energies within the perovskite bandgap; this was attributed to the ionic bonding of the perovskite. This implies Schottky defects are unlikely to be effective as non-radiative recombination centres. Elemental defects, such as Pb, I and CH₃NH₃ vacancies associated with Frenkel defects, were found to form shallow levels near band edges, again reducing the effectiveness as non-radiative recombination centres. However, these conclusions may need to be moderated by the well-known limitations of density functional theory studies^{14,45}. Another recent study⁶³ that used a similar approach reached similar conclusions. Dominant defects in the iodide are deduced to be p-type Pb vacancies and n-type methylammonium interstitials, with growth conditions determining the final doping polarity. This study also considered anti-site substitutions, which, along with Pb interstitials, formed states near the middle of the bandgap. However, formation energies were high, meaning that these defects are expected to form in low concentrations at the relatively low material deposition temperature involved. Although experimental confirmation is required, these results may help explain

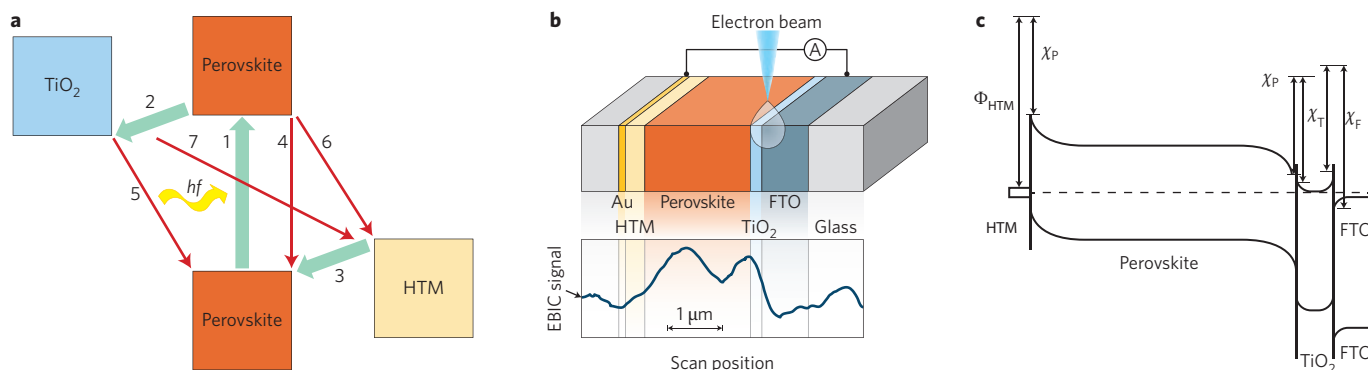


Figure 4 | Electron-transfer processes in nanoparticle and bulk cells together with a bulk energy-band diagram. **a**, Schematic of electron-transfer processes in a perovskite nanoparticle or ETA device⁷¹. The thick green and thin red arrows respectively indicate the processes desirable for energy conversion and those associated with losses. hf , photon energy. **b**, Schematic of EBIC experiment⁷². A scanned electron beam generates a cloud of carriers, creating a position-dependent current in a short-circuiting load. **c**, Energy-band diagram deduced from the vacuum energy levels shown in Fig. 2b. χ_P , χ_T and χ_F represent the electron affinities of the perovskite, TiO₂ and FTO layers, respectively, and Φ_{HTM} represents the work function of the HTM layer. (The barrier at the TiO₂/FTO interface has been a source of discussion in the dye-cell literature^{97,98}, because it impedes carrier collection in the direction shown. Some work suggests states generated at the interface under white-light illumination cause a pinning effect, reducing its significance⁹⁸. Other work suggests a failure of the Anderson rule, which is not uncommon, and that the barrier has the opposite direction at thermal equilibrium⁹⁹.)

why high-performance perovskite cells can be produced by a diverse range of deposition approaches and a wide variety of cell structures.

Although the dielectric properties of perovskites have not yet been shown to be important for good performance, they are so extreme compared to those of conventional semiconductors that it is a possibility. Figure 3b shows a composite of reported data obtained at 300 K for CH₃NH₃PbI₃. At low frequencies, the dielectric constant is large; it has been reported to be 60.9 over the 20 Hz – 1 MHz range⁶⁴, which is consistent with the low-frequency value of 60.2 obtained from fits at higher frequencies⁶⁵. This low-frequency value is appropriate in determining steady-state properties, with static fields consequently varying slowly with position — five times slower than in silicon under similar electrostatic disturbances. The high value of the dielectric constant results from a combination of dipolar, ionic and electronic contributions. As the excitation frequency increases, the permanent dipole associated with the organic cation can no longer respond and a new plateau is reached with a dielectric constant of 29.7 (ref. 65). Finally, at infrared frequencies, the ionic component drops out, leaving only the electronic response. The dielectric constant drops to 6.5 at optical frequencies⁶⁶, lower than that of inorganic semiconductors with a similar bandgap. The dashed lines in Fig. 3b indicate possible transition values of the constants.

The other possibility is that CH₃NH₃PbI₃ may possess paraelectric or even ferroelectric properties at room temperature and above, impacting device performance^{67,68}. The main evidences for this is the hysteresis observed in resistivity measurements, which is not seen in related compounds prepared similarly, and the remnant polarization, which is apparent as a finite voltage output at zero current²⁹. The crystallographic point group ($4mm$) of both the room-temperature and high-temperature iodide phases is consistent with ferroelectric behaviour²⁹. Hysteresis has also been reported for high-efficiency devices^{69,70}, although many other explanations are also possible for this besides ferroelectric effects⁶⁹. Best performance has been realized when hysteresis is minimized (S. I. Seok, personal communication). Carrier collection along the boundaries of microscopic ferroelectric domains has also been suggested⁶⁸, although this presently lacks experimental support.

Device operation

High efficiencies have been realized using a diverse range of operating modes, spanning from generation and collection at sparse

points on the surfaces of titania nanoparticles²⁶ to conventional planar thin-film operation³².

In the dye-sensitized and ETA configurations, perovskites are not required to have good carrier transport, as the interfacial properties mainly determine the performance (Fig. 4a depicts the key processes involved⁷¹). The desirable processes involve photoexcitation in perovskite (1), electron transfer to titania (2) and hole transfer to the HTM (3) (or, equivalently, electron transfer from the HTM to the perovskite). Undesirable processes are recombination of photogenerated species (4), back charge transfer at the interfaces of TiO₂ and the HTM with the perovskite (5,6) and between TiO₂ and the HTM (7) (this may occur if perovskite is absent in some areas — for example, when nanoparticles or voids are present). For high performance, processes (4)–(7) must operate on much slower timescales than charge generation and extraction (1)–(3). Time-resolved transient techniques have proved useful for studying the related kinetics⁷².

For thicker perovskite layers, photogenerated carrier transport becomes important. Initial data suggested that the mixed halide CH₃NH₃PbI_{3-x}Cl_x has a distinct advantage over the pure iodide — its carrier diffusion length (>1 μm ; ref. 73) is about ten times greater than that (about 100 nm) of the pure iodide^{73,74}. Subsequent work with the iodide prepared by the vapour-phase CH₃NH₃I conversion of PbI₂ resulted in good carrier collection in 350-nm-thick iodide films, suggesting that the diffusion lengths exceed this thickness³⁴; this is supported by recent electron-beam measurements⁶⁰.

Recently, collection across a film cross-section has been directly probed using the electron beam induced current (EBIC) technique (Fig. 4b)^{60,72}. In this technique, the electron beam generates a cloud of excited carriers (these are expected to be largely free electron-hole pairs, some of which may combine to form excitons if they have short association times). Because the resolution is limited by the size of this cloud, approximately 1,500-nm-thick perovskite layers were grown, which are appreciably thicker than those in optimal planar cells.

The typical line scan shown in Fig. 4b has two interesting features. The first is the double peak in the EBIC signal within the perovskite. This indicates the cell's ambipolar response with carriers generated both near the spiro-MeOTAD HTM and near the ETM (TiO₂ plus FTO) being collected. The second interesting feature is the dip between the two peaks, which arises because an appreciable fraction of the generated carriers recombine on their way to their preferred contact, due to the sample thickness exceeding the optimal thickness.

These features can be understood by constructing the expected thermal-equilibrium energy-band diagram of the device from the vacuum energy levels shown in Fig. 2b. At thermal equilibrium, a common Fermi level prevails throughout the device. A first-order estimate of how the energies within the different materials align when brought together is possible by the combined use of the Anderson rule for semiconductor heterojunctions⁷⁵ and the related Schottky–Mott rule for metal–semiconductor interfaces. Both are known to have severe limitations, but they have the advantage over more sophisticated approaches⁷⁶ of being universal in application. In both rules, the vacuum reference level is assumed to be continuous across material interfaces. For semiconductors, this means that the relative alignment of conduction band edges across interfaces depends on the difference of the electron affinities of the two materials (the energy from the conduction band edge to the vacuum level). For metal–semiconductor interfaces, the conduction band edge will lie above the metal Fermi level by an energy equal to the metal work function minus the semiconductor electron affinity.

Applying these two rules and treating the HTM as a metal gives the energy-band diagram shown in Fig. 4c for the case when the perovskite layer is reasonably thick. The associated potential variations across the perovskite are due to the low work function of the compact TiO₂ layer (doped at about 10^{18} – 10^{19} cm⁻³, ref. 77) compared to the HTM layer. Background perovskite doping levels are low (they are commonly estimated to be $\sim 10^{14}$ – 10^{16} cm⁻³; resistivity and Seebeck coefficient measurements²⁹ suggest even lower values, but they are probably dependent on preparation conditions). This results in the build up of holes near the HTM and electrons near the ETM (their concentrations equal the product of the effective density of states in the respective band and the negative exponential of the difference between the Fermi level and this band edge normalized by the thermal energy, kT , where k is the Boltzmann constant and T is the absolute temperature). The slope of either band edge gives the local electric field, which is strongest near the HTM and the ETM. For thick devices, these high-field regions may be independent of each other (as shown in Fig. 4c), whereas they merge for thin devices, eventually creating an essentially uniform field across the device. With increasing device voltage, the high-field regions tend to decouple.

The EBIC outputs are low short-circuit currents, which is consistent with the use of small-signal calculations in which a thermal-equilibrium equivalent circuit is used to model carrier drift and diffusion⁷⁸. The low response when the beam is centred at the HTM/perovskite interface is probably because of a high electron recombination velocity at this interface, corresponding to the back charge-transfer process (6) in Fig. 4a. This velocity needs to be lower than the drift velocity of electrons to prevent the formation of a dead layer near this interface⁷⁸. The response at the TiO₂–perovskite interface is much higher, suggesting that there is no dead layer near this interface and that carrier generation in the TiO₂ itself might contribute to the EBIC signal. The higher peak value on the HTM side of the device may correspond to a more extended high-field region on this side as a result of the band alignment imposed at the HTM interface.

Recent work^{79,80} has allowed the accuracy of the Anderson and Schottky–Mott rules used for deducing Fig. 4c to be assessed. Lindblad *et al.*⁷⁹ found that the alignment between the occupied valence bands of iodide perovskite and nanoporous TiO₂ was 2.1 eV using hard-X-ray photoelectron spectroscopy. Using ultraviolet photoemission spectroscopy and inverse photoemission spectroscopy to respectively interrogate occupied and unoccupied states, Schulz *et al.*⁸⁰ self-consistently deduced the work functions, electron affinities and valence-band maxima. Moreover, all measurements were conducted in the same ultrahigh vacuum for compact uncoated TiO₂ samples, TiO₂ samples coated with iodide, bromide and mixed chloride perovskites, and for the latter samples overlaid with different thicknesses of the HTM. The final picture

obtained is roughly consistent with that shown in Fig. 4c. TiO₂ and the perovskite were deduced to have similar electron affinities, as shown. Undoped spiro-MeOTAD was used in the study⁸⁰ with the alignments deduced consistent with those in Fig. 4c for the doped material.

Commercialization challenges

A series of unsuccessful attempts to commercialize new solar-cell technology in recent years vividly demonstrates the non-trivial challenges of commercialization. A key prerequisite for commercialization is a compelling market advantage over incumbent technologies. For perovskites, such an advantage might be low processing costs, high conversion efficiencies through tandem device structures or unique products, such as the above-mentioned flexible or partially transparent modules. The present reliance on Pb as a key perovskite component may militate against the adoption of such products in consumer or building integrated applications. The present relative lack of robustness may present an additional barrier for mainstream bulk power applications.

In terms of cost, the closest commercial technology that perovskites must compete with is CdTe, the photovoltaic thin-film technology with the lowest production cost. Fabrication is by simple vapour-phase deposition onto FTO-coated glass with a ‘glass in’ to ‘module out’ time of 2.5 h (ref. 81). Semiconductor costs are low, with Te currently costing <\$115 kg⁻¹. Other material costs (such as those of FTO-coated glass sheets, junction boxes, tabbing, encapsulants, sealants and tempered glass backsheets) account for most of the manufacturing cost, which was reported to be US\$0.54 W⁻¹ in the final quarter of 2013 or US\$72 m⁻² at an average module conversion efficiency of 13.4% (ref. 82). There is considered to be limited potential for reducing the cost per unit area, which is primarily determined by the above-mentioned material costs; US\$68 m⁻² is the target for the end of 2017⁸³. This reduction in conjunction with a predicted increase in the average module efficiency to 17.2% over this timeframe⁸⁴ is anticipated to reduce the manufacturing cost to US\$0.38–0.41 W⁻¹ by 2017, which is slightly higher than the projected manufacturing costs for mainstream Si-based modules produced by leading manufacturers⁸⁵.

Although perovskite modules could arguably be processed more simply than CdTe modules, this is unlikely to greatly affect the cost per unit area, because their overall cost is mainly determined by the costs of the mostly common materials. In fact, perovskite modules may require more expensive encapsulation to overcome their present relatively low robustness. Consequently, perovskite modules would need to at least match the projected efficiencies of CdTe modules to gain a competitive advantage over them. This may just be possible with single cells, for which both technologies appear capable of achieving efficiencies of over 20%. The opportunity for perovskite modules could lie with tandem cells, where a clear efficiency advantage over CdTe appears feasible without greatly affecting the manufacturing cost per unit area but significantly decreasing the cost per watt.

The present perovskites share a common disadvantage with CdTe, namely reliance on an environmentally hazardous heavy metal. Apart from in Japan and for specific applications (such as residential rooftops), the toxicity of CdTe appears to have had minimal impact on market acceptance to date. Photovoltaic modules are presently exempted from legislation such as the European Restriction on Hazardous Substances (RoHS)⁸⁶, at least for large, stationary, professionally installed systems. Without this exemption, CdTe modules would have no possibility of meeting the RoHS requirement of having less than 0.01% Cd by weight in any homogeneous layer (defined as a layer of “uniform composition throughout” or one “that cannot be ... separated into different materials by mechanical actions such as unscrewing, cutting, crushing, grinding and abrasive processes”⁸⁶). Modules based on present perovskites

fare better, as the RoHS limit on Pb in a homogeneous layer is ten times higher than that for Cd, but they also appear to have no prospects for compliance if they contain the optional continuous layer shown in Fig. 2a. If the scaffold layer were accepted as a homogeneous layer, the Pb content would be diluted in both nanoparticle-sensitized and ETA devices. (If 18 2.5-nm-diameter hemispherical iodide perovskite nanoparticles coat a 20-nm-diameter TiO₂ nanosphere²¹, the scaffolding layer has a porosity of 60% and the pores are filled by spiro-MeOTAD, the Pb content will be 0.4–0.5% by weight, which exceeds the RoHS limit, although not appreciably). Cd and Pb compounds have different solubilities⁵, which does not affect compliance with RoHS criteria, but it may affect end-of-life disposal.

The low robustness of present perovskite technology to moist air and water vapour means that out of all the present commercial photovoltaic technologies it is most closely related to CIGS. Unencapsulated CIGS cells generally degrade during damp heat testing, although this can be controlled to acceptable levels by employing suitable encapsulation. A recent study investigating the feasibility of encapsulating CIGS cells in flexible modules concluded that 'breathable' designs are not viable^{87,88}. Layers that effectively restrict water ingress are required together with internal encapsulant layers with a high moisture solubility to keep their relative moisture saturation low. Double glass layers are used in present commercial CIGS modules together with edge sealants, both of which effectively prevent moisture penetration^{89,90}. Alternative approaches, such as integrating moisture barriers like Al₂O₃ into the device structure, might eventually eliminate the need to use such restricted designs for perovskite⁹¹ and CIGS⁹² cells. Degradation under ultraviolet exposure, which is reportedly more severe for devices with TiO₂ scaffolding, may similarly be addressed by protective encapsulation features (in this case, ultraviolet filtering) or device design⁹³.

Summary and future prospects

The next few years promise to be exciting ones for research and development of organic–inorganic halide perovskite solar cells. On-going efficiency improvements are expected, as well as a rapidly growing understanding of their material properties and optimal cell designs.

Advantages over existing photovoltaic technologies include material properties that simplify the manufacture of high-performance devices. The diversity in demonstrated approaches may give rise to low processing costs and simple implementation of attractive products, such as flexible, transparent or all-perovskite tandem cell modules. This diversity may also allow perovskite cells to be directly integrated with other cell technologies to form high-performance tandem cells; Si and CIGS modules appear particularly promising in this respect^{3,6}.

In the present market, the toxicity of Pb is not a major impediment to large-scale, professional applications, as is evidenced by the fact that CdTe cells have already gained a reasonable market share. Cd or Pb is also present in some CIGS and silicon modules at the same general level as that likely in perovskite modules⁹⁴. The danger is that technology relying on toxic materials may be increasingly marginalized as legislation becomes increasingly more pervasive and restrictive. Elimination of Pb seems the only sure solution, with replacement by Sn a possibility⁹⁵. Alternatively, research into the present perovskites might allow more precise determination of the features that have resulted in such rapid progress, encouraging identification and investigation of non-toxic material systems with similar properties.

The recent surge in interest makes it likely there will be multiple attempts to commercialize perovskite photovoltaic products in coming years. Perovskites have the advantage that they provide multiple paths to commercialization. As well as the traditional approach of challenging established manufacturers, there is also the opportunity to work with these to develop high-performance tandem cell

technology that uses both perovskite and existing technologies; this may allow market introduction as a new premium product.

Received 10 February 2014; accepted 12 May 2014; published online 27 June 2014

References

1. Turner, G. Global Renewable Energy Market Outlook 2013. *Bloomberg New Energy Finance* <https://www.bnef.com/insightdownload/7526/pdf> (11 April 2014).
2. Park, N.-G. Organometal perovskite light absorbers toward a 20% efficiency low-cost solid-state mesoscopic solar cell. *J. Phys. Chem. Lett.* **4**, 2423–2429 (2013).
3. Snaith, H. J. Perovskites: the emergence of a new era for low-cost, high-efficiency solar cells. *J. Phys. Chem. Lett.* **4**, 3623–3630 (2013).
4. Kim, H.-S., Im, S. H. & Park, N.-G. Organolead halide perovskite: new horizons in solar cell research. *J. Phys. Chem. C* **118**, 5615–5625 (2014).
5. Hodes, G. & Cahen, D. Photovoltaics: perovskite cells roll forward. *Nature Photon.* **8**, 87–88 (2014).
6. Service, R. F. Perovskite solar cells keep on surging. *Science* **344**, 458 (2014).
7. Li, C. *et al.* Formability of ABX₃ (X = F, Cl, Br, I) halide perovskites. *Acta Crystallogr. B* **64**, 702–707 (2008).
8. McKinnon, N. K., Reeves, D. C. & Akabas, M. H. 5-HT₃ receptor ion size selectivity is a property of the transmembrane channel, not the cytoplasmic vestibule portals. *J. Gen. Physiol.* **138**, 453–466 (2011).
9. Cohen, B. N., Labarca, C., Davidson, N. & Lester, H. A. Mutations in M2 alter the selectivity of the mouse nicotinic acetylcholine receptor for organic and alkali metal cations. *J. Gen. Physiol.* **100**, 373–400 (1992).
10. Im, J.-H., Chung, J., Kim, S.-J. & Park, N.-G. Synthesis, structure, and photovoltaic property of a nanocrystalline 2H perovskite-type novel sensitizer (CH₃CH₂NH₃)PbI₃. *Nanoscale Res. Lett.* **7**, 353 (2012).
11. Koh, T. M. *et al.* Formamidinium-containing metal-halide: an alternative material for near-IR absorption perovskite solar cells. *J. Phys. Chem. C* <http://dx.doi.org/10.1021/jp411112k> (13 December 2013).
12. Eperon, G. E. *et al.* Formamidinium lead trihalide: a broadly tunable perovskite for efficient planar heterojunction solar cells. *Energy Environ. Sci.* **7**, 982–988 (2014).
13. Pang, S. *et al.* NH₂CH=NH₂PbI₃: An alternative organolead iodide perovskite sensitizer for mesoscopic solar cells. *Chem. Mater.* **26**, 1485–1491 (2014).
14. Umari, P., Mosconi, E. & De Angelis, F. Relativistic GW calculations on CH₃NH₃PbI₃ and CH₃NH₃SnI₃ perovskites for solar cell applications. *Sci. Rep.* **4**, 4467 (2014).
15. Topsøe, H. Kristallografisch-chemische untersuchungen homologer verbindungen. *Zeitschrift für Kristallographie* **8**, 246–296 (1884).
16. Mitzi, D. B., Wang, S., Feild, C. A., Chess, C. A. & Guloy, A. M. Conducting layered organic–inorganic halides containing <110>-oriented perovskite sheets. *Science* **267**, 1473–1476 (1995).
17. Mitzi, D. B., Chondroudis, K. & Kagan, C. R. Organic–inorganic electronics. *IBM J. Res. Dev.* **45**, 29–45 (2001).
18. Kojima, A., Teshima, K., Miyasaka, T. & Shirai, Y. Novel photoelectrochemical cell with mesoscopic electrodes sensitized by lead-halide compounds (2). in *Proc. 210th ECS Meeting* (ECS, 2006).
19. Kojima, A., Teshima, K., Shirai, Y. & Miyasaka, T. Organometal halide perovskites as visible-light sensitizers for photovoltaic cells. *J. Am. Chem. Soc.* **131**, 6050–6051 (2009).
20. Kojima, A., Teshima, K., Shirai, Y. & Miyasaka, T. Novel photoelectrochemical cell with mesoscopic electrodes sensitized by lead-halide compounds (11). in *Proc. 214th ECS Meeting* (ECS, 2014).
21. Im, J.-H., Lee, C.-R., Lee, J.-W., Park, S.-W. & Park, N.-G. 6.5% efficient perovskite quantum-dot-sensitized solar cell. *Nanoscale* **3**, 4088–4093 (2011).
22. Kim, H.-S. *et al.* Lead iodide perovskite sensitized all-solid-state submicron thin film mesoscopic solar cell with efficiency exceeding 9%. *Sci. Rep.* **2**, 591 (2012).
23. Lee, M. M., Teuscher, J., Miyasaka, T., Murakami, T. N. & Snaith, H. J. Efficient hybrid solar cells based on meso-superstructured organometal halide perovskites. *Science* **338**, 643–647 (2012).
24. Salbeck, J., Yu, N., Bauer, J., Weissörtel, F. & Bestgen, H. Low molecular organic glasses for blue electroluminescence. *Synthetic Metals* **91**, 209–215 (1997).
25. Bach, U. *et al.* Solid-state dye-sensitized mesoporous TiO₂ solar cells with high photon-to-electron conversion efficiencies. *Nature* **395**, 583–585 (1998).
26. Stranks, S. D. *et al.* Electron–hole diffusion lengths exceeding 1 micrometer in an organometal trihalide perovskite absorber. *Science* **342**, 341–344 (2013).
27. Heo, J. H. *et al.* Efficient inorganic–organic hybrid heterojunction solar cells containing perovskite compound and polymeric hole conductors. *Nature Photon.* **7**, 486–491 (2013).

28. Noh, J. H., Im, S. H., Heo, J. H., Mandal, T. N. & Seok, S. I. Chemical management for colorful, efficient, and stable inorganic-organic hybrid nanostructured solar cells. *Nano Lett.* **13**, 1764–1769 (2013).
29. Stoumpos, C. C., Malliakas, C. D. & Kanatzidis, M. G. Semiconducting tin and lead iodide perovskites with organic cations: phase transitions, high mobilities, and near-infrared photoluminescent properties. *Inorg. Chem.* **52**, 9019–9038 (2013).
30. Burschka, J. *et al.* Sequential deposition as a route to high-performance perovskite-sensitized solar cells. *Nature* **499**, 316–319 (2013).
31. Green, M. A., Emery, K., Hishikawa, Y., Warta, W. & Dunlop, E. D. Solar cell efficiency tables (version 43). *Prog. Photovolt.* **22**, 1–9 (2014).
32. Liu, M., Johnston, M. B. & Snaith, H. J. Efficient planar heterojunction perovskite solar cells by vapour deposition. *Nature* **501**, 395–398 (2013).
33. Burschka, J. High performance solid-state mesoscopic solar cells. PhD thesis, *École Polytechnique Fédérale de Lausanne* 107 (2013).
34. Chen, Q. *et al.* Planar heterojunction perovskite solar cells via vapor-assisted solution process. *J. Am. Chem. Soc.* **136**, 622–625 (2014).
35. Liu, D. & Kelly, T. L. Perovskite solar cells with a planar heterojunction structure prepared using room-temperature solution processing techniques. *Nature Photon.* **8**, 133–138 (2014).
36. Christians, J. A., Fung, R. C. M. & Kamat, P. V. An inorganic hole conductor for organo-lead halide perovskite solar cells. Improved hole conductivity with copper iodide. *J. Am. Chem. Soc.* **136**, 758–764 (2014).
37. Ito, S. Pb perovskite solar cells using inorganic hole conductor of CuSCN. Paper Y-RS-14 in 2013 MRS Fall Meeting & Exhibit (MRS, 2013).
38. Docampo, P., Ball, J. M., Darwich, M., Eperon, G. E. & Snaith, H. J. Efficient organometal trihalide perovskite planar-heterojunction solar cells on flexible polymer substrates. *Nature Commun.* **4**, 2761 (2013).
39. Malinkiewicz, O. *et al.* Perovskite solar cells employing organic charge-transport layers. *Nature Photon.* **8**, 128–132 (2014).
40. Sun, S. *et al.* The origin of high efficiency in low-temperature solution-processable bilayer organometal halide hybrid solar cells. *Energy Environ. Sci.* **7**, 399–407 (2014).
41. Wang, J. T.-W. *et al.* Low-temperature processed electron collection layers of graphene/TiO₂ nanocomposites in thin film perovskite solar cells. *Nano Lett.* **14**, 724–730 (2014).
42. Wojciechowski, K., Saliba, M., Leijtens, T., Abate, A. & Snaith, H. J. Sub-150 °C processed meso-superstructured perovskite solar cells with enhanced efficiency. *Energy Environ. Sci.* **7**, 1142–1147 (2014).
43. Eperon, G. E., Burlakov, V. M., Goriely, A. & Snaith, H. J. Neutral color semitransparent microstructured perovskite solar cells. *ACS Nano* **8**, 591–598 (2014).
44. Wang, J. *et al.* Performance improvement of amorphous silicon see-through solar modules with high transparency by the multi-line ns-laser scribing technique. *Opt. Las. Eng.* **51**, 1206–1212 (2013).
45. Even, J., Pedesseau, L., Jancu, J.-M. & Katan, C. Importance of spin-orbit coupling in hybrid organic/inorganic perovskites for photovoltaic applications. *J. Phys. Chem. Lett.* **4**, 2999–3005 (2013).
46. Sell, D. D. & Lawaetz, P. New analysis of direct exciton transitions: application to GaP. *Phys. Rev. Lett.* **26**, 311–314 (1971).
47. Even, J., Pedesseau, L., Dupertuis, M.-A., Jancu, J.-M. & Katan, C. Electronic model for self-assembled hybrid organic/perovskite semiconductors: reverse band edge electronic states ordering and spin-orbit coupling. *Phys. Rev. B* **86**, 205301 (2012).
48. Ishihara, T. Optical properties of PbI₂-based perovskite structures. *J. Luminescence* **60**, 269–274 (1994).
49. D'Innocenzo, V. *et al.* Excitons versus free charges in organo-lead tri-halide perovskites. *Nature Commun.* **5**, 3586 (2014).
50. Tauc, J. Optical properties and electronic structure of amorphous Ge and Si. *Mater. Res. Bull.* **3**, 37–46 (1968).
51. Elliott, R. J. Intensity of optical absorption by excitons. *Phys. Rev.* **108**, 1384–1389 (1957).
52. Tanaka, K. *et al.* Comparative study on the excitons in lead-halide-based perovskite-type crystals CH₃NH₃PbBr₃, CH₃NH₃PbI₃. *Solid State Commun.* **127**, 619–623 (2003).
53. Combescot, M. Thermodynamics of an electron-hole system in semiconductors. *Phys. Status Solidi B* **86**, 349–358 (1978).
54. Corkish, R., Chan, D. S.-P. & Green, M. A. Excitons in silicon diodes and solar cells: a three-particle theory. *J. Appl. Phys.* **79**, 195–203 (1996).
55. Geelhaar, F. *Coulomb Correlation Effects in Silicon Devices* (Series in Microelectronics 147 Hartung-Gorre, 2004).
56. Green, M. A. Many-body theory applied to solar cells: excitonic and related carrier correlation effects in *Proc. 26th IEEE Photovoltaic Specialists Conference* (1997).
57. Green, M. A. Radiative efficiency of state-of-the-art photovoltaic cells. *Prog. Photovolt.* **20**, 472–476 (2012).
58. Ungár, T. The meaning of size obtained from broadened X-ray diffraction peaks. *Adv. Eng. Mater.* **5**, 323–329 (2003).
59. Edalati, K. & Horita, Z. Significance of homologous temperature in softening behavior and grain size of pure metals processed by high-pressure torsion. *Mater. Sci. Eng. A* **528**, 7514–7523 (2011).
60. Edri, E. *et al.* Why lead methylammonium tri-iodide perovskite-based solar cells require a mesoporous electron transporting scaffold (but not necessarily a hole conductor). *Nano Lett.* **14**, 1000–1004 (2014).
61. Liang, K., Mitzi, D. B. & Prikas, M. T. Synthesis and characterization of organic-inorganic perovskite thin films prepared using a versatile two-step dipping technique. *Chem. Mater.* **10**, 403–411 (1998).
62. Kim, J., Lee, S.-H., Lee, J. H. & Hong, K.-H. The role of intrinsic defects in methylammonium lead iodide perovskite. *J. Phys. Chem. Lett.* **5**, 1312–1317 (2014).
63. Yin, W.-J., Shi, T. & Yan, Y. Unusual defect physics in CH₃NH₃PbI₃ perovskite solar cell absorber. *Appl. Phys. Lett.* **104**, 063903 (2014).
64. Onoda-Yamamuro, N., Matsuo, T. & Suga, H. Dielectric study of CH₃NH₃PbX₃ (X = Cl, Br, I). *J. Phys. Chem. Solids* **53**, 935–939 (1992).
65. Poglitsch, A. & Weber, D. Dynamic disorder in methylammoniumtrihalogenoplumbates (II) observed by millimeter-wave spectroscopy. *J. Chem. Phys.* **87**, 6373 (1987).
66. Hirasawa, M., Ishihara, T., Goto, T., Uchida, K. & Miura, N. Magnetoabsorption of the lowest exciton in perovskite-type compound (CH₃NH₃)PbI₃. *Physica B* **201**, 427–430 (1994).
67. Yuan, Y., Xiao, Z., Yang, B. & Huang, J. Arising applications of ferroelectric materials in photovoltaic devices. *J. Mater. Chem. A* **2**, 6027–6041 (2014).
68. Frost, J. M. *et al.* Atomistic origins of high-performance in hybrid halide perovskite solar cells. *Nano Lett.* **14**, 2584–2590 (2014).
69. Snaith, H. J. *et al.* Anomalous hysteresis in perovskite solar cells. *J. Phys. Chem. Lett.* **5**, 1511–1515 (2014).
70. Hoke, E. T., Unger, E. L., Vandewal, K. & McGehee, M. D. Charge recombination and transport in hybrid perovskite solar cells: why do perovskite solar cells have large Voc? in *Proc. MRS Fall Meeting and Exhibit* (2013).
71. Marchioro, A. *et al.* Unravelling the mechanism of photoinduced charge transfer processes in lead iodide perovskite solar cells. *Nature Photon.* **8**, 250–255 (2014).
72. Edri, E. *et al.* Elucidating the charge carrier separation mechanism in CH₃NH₃PbI_{3-x}Cl_x perovskite solar cells. *Nature Commun.* **5**, 3461 (2014).
73. Stranks, S. D. *et al.* Electron-hole diffusion lengths exceeding 1 micrometer in an organometal trihalide perovskite absorber. *Science* **342**, 341–344 (2013).
74. Xing, G. *et al.* Long-range balanced electron- and hole-transport lengths in organic-inorganic CH₃NH₃PbI₃. *Science* **342**, 344–347 (2013).
75. Anderson, R. L. Germanium-gallium arsenide heterojunction. *IBM J. Res. Dev.* **4**, 283–287 (1960).
76. Peressi, M., Baldereschi, A. & Baroni, S. in *Characterization of Semiconductor Heterostructures and Nanostructures* 2nd Edn (eds Agostini G. & Lamberti, C) Ch. 2 (Elsevier, 2008).
77. Kavan, L. & Grätzel, M. Highly efficient semiconducting TiO₂ photoelectrodes prepared by aerosol pyrolysis. *Electrochimica Acta* **40**, 643–652 (1995).
78. Green, M. A. The depletion layer collection efficiency for *p-n* junction, Schottky diode, and surface insulator solar cells. *J. Appl. Phys.* **47**, 547–554 (1976).
79. Lindblad, R. *et al.* Electronic structure of TiO₂/CH₃NH₃PbI₃ perovskite solar cell interfaces. *J. Phys. Chem. Lett.* **5**, 648–653 (2014).
80. Schulz, P. *et al.* Interface energetics in organo-metal halide perovskite-based photovoltaic cells. *Energy Environ. Sci.* **7**, 1377–1381 (2014).
81. *First Solar Sets New World Record for CdTe Solar Cell Efficiency*. <http://investor.firstsolar.com/releasedetail.cfm?releaseid=743398> (26 February 2013).
82. Widmar, M. *First Solar Q4'13 Earnings Call*. http://files.shareholder.com/downloads/fslr/1347979521x0x728649/bddf430-a025-43e4-8b91-c1915066b274/q413_earnings_call_presentation_final1.pdf (25 February 2014).
83. De Jong, T. *First Solar Manufacturing Update*. http://files.shareholder.com/downloads/fslr/3084163747x0x652323/53f7a04f-fcf5-4729-8bb2-0abf6033c046/4.%20fsanalystday_manufacturing.pdf (11 April 2014).
84. Garabedian, R. *Technology Update. 2013 Analyst Meeting, First Solar*. http://files.shareholder.com/downloads/FSLR/3084163747x0x652328/d0af6554-e193-47e4-9dd0-59b02968272b/fsanalystday_technologyupdate.pdf (11 April 2014).
85. Rinaldi, N. *Solar PV Module Costs to Fall to 36 Cents per Watt by 2017* <http://www.greentechmedia.com/articles/read/solar-pv-module-costs-to-fall-to-36-cents-per-watt> (18 June 2013).
86. Directive 2011/65/EU of the European Parliament and of the Council of 8 June 2011 on the restriction of the use of certain hazardous substances in electrical and electronic equipment (recast). <http://eur-lex.europa.eu/legal-content/en/TXT/?uri=celex:32011L0065> (8 June 2011).

87. Coyle, D. J. Life prediction for CIGS solar modules part 1: modeling moisture ingress and degradation. *Prog. Photovolt.* **21**, 156–172 (2013).
88. Coyle, D. J. *et al.* Life prediction for CIGS solar modules part 2: degradation kinetics, accelerated testing, and encapsulant effects. *Prog. Photovolt.* **21**, 173–186 (2013).
89. Kempe, M. D., Dameron, A. A. & Reese, M. O. Evaluation of moisture ingress from the perimeter of photovoltaic modules. *Prog. Photovolt.* <http://dx.doi.org/10.1002/pip.2374> (2013).
90. Kempe, M. D., Panchagade, D., Reese, M. O. & Dameron, A. A. Modeling moisture ingress through polyisobutylene-based edge-seals. *Prog. Photovolt.* <http://dx.doi.org/10.1002/pip.2465> (2014).
91. Niu, G. *et al.* Study on the stability of $\text{CH}_3\text{NH}_3\text{PbI}_3$ films and the effect of post-modification by aluminum oxide in all-solid-state hybrid solar cells. *J. Mater. Chem. A* **2**, 705–710 (2014).
92. Garcia, P. F., McLean, R. S. & Hegedus, S. ALD Moisture barrier for Cu(InGa)Se₂ solar cells. in *Proc. 218th ECS Meeting* (ECS, 2010).
93. Leijtens, T. *et al.* Overcoming ultraviolet light instability of sensitized TiO₂ with meso-superstructured organometal tri-halide perovskite solar cells. *Nature Commun.* **4**, 2885 (2013).
94. Werner, J. H., Zapf-Gottwick, R., Koch, M. & Fischer, K. Toxic substances in photovoltaic modules. in *Proc. 21st Int. Photovoltaic Sci. Eng. Conf.* (2011).
95. Noel, N. K. *et al.* Lead-free organic-inorganic tin halide perovskites for photovoltaic applications. *Energy Environ. Sci.* <http://dx.doi.org/10.1039/c4ee01076K> (2014).
96. Wehrenfennig, C., Liu, M., Snaith, H. J., Johnston, M. B. & Herz, L. M. Homogeneous emission line broadening in the organo lead halide perovskite $\text{CH}_3\text{NH}_3\text{PbI}_{3-x}\text{Cl}_x$. *J. Phys. Chem. Lett.* **5**, 1300–1306 (2014).
97. Rühle, S. & Dittrich, T. Investigation of the electric field in TiO₂/FTO junctions used in dye-sensitized solar cells by photocurrent transients. *J. Phys. Chem. B* **109**, 9522–9526 (2005).
98. Snaith, H. J. & Grätzel, M. The role of a “Schottky barrier” at an electron-collection electrode in solid-state dye-sensitized solar cells. *Adv. Mater.* **18**, 1910–1914 (2006).
99. Kron, G., Rau, U. & Werner, J. H. Influence of the built-in voltage on the fill factor of dye-sensitized solar cells. *J. Phys. Chem. B* **107**, 13258–13261 (2003).

Acknowledgements

The Australian Centre for Advanced Photonics (ACAP) is supported by the Australian Government through the Australian Renewable Energy Agency (ARENA). Responsibility for the views, information or advice expressed herein is not accepted by the Australian Government. H.J.S. is supported by the Engineering and Physical Sciences Research Council UK and the European Research Council.

Additional information

Reprints and permissions information is available at www.nature.com/reprints. Requests for materials and correspondence should be addressed to M.A.G.

Competing financial interests

The authors declare no financial interests.